electronic reprint

Journal of
Synchrotron Radiation
ISSN 0909-0495
Editors: **Å. Kvick, D. M. Mills and T. Ohta**

Analog pixel array detectors

A. Ercan, M. W. Tate and S. M. Gruner

Journal of
Synchrotron Radiation
ISSN 0909-0495

Received 21 June 2005
Accepted 10 September 2005

Analog pixel array detectors

A. Ercan,[a,b] M. W. Tate[b,c] and S. M. Gruner[b,c,d]*

[a]School of Applied and Engineering Physics, Cornell University, Ithaca, NY 14853, USA, [b]Laboratory of Atomic and Solid State Physics, Cornell University, Ithaca, NY 14853, USA, [c]Physics Department, Cornell University, Ithaca, NY 14853, USA, and [d]Cornell High Energy Synchrotron Source (CHESS), Cornell University, Ithaca, NY 14853, USA. E-mail: smg26@cornell.edu

X-ray pixel array detectors (PADs) are generally thought of as either digital photon counters (DPADs) or X-ray analog-integrating pixel array detectors (APADs). Experiences with APADs, which are especially well suited for X-ray imaging experiments where transient or high instantaneous flux events must be recorded, are reported. The design, characterization and experimental applications of several APAD designs developed at Cornell University are discussed. The simplest design is a 'flash' architecture, wherein successive integrated X-ray images, as short as several hundred nanoseconds in duration, are stored in the detector chips for later off-chip digitization. Radiography experiments using a prototype flash APAD are summarized. Another design has been implemented that combines flash capability with the ability to continuously stream X-ray images at slower (*e.g.* milliseconds) rates. Progress is described towards radiation-hardened APADs that can be tiled to cover a large area. A mixed-mode PAD, design by combining many of the attractive features of both APADs and DPADs, is also described.

Keywords: X-ray detector; area detector; time-resolved radiography.

1. Introduction

Synchrotron radiation X-ray sources provide sufficient flux to enable X-ray diffraction, crystallography and radiography experiments on microsecond and submicrosecond time scales. Experiments of interest include complex biological, chemical and physical interactions, such as enzyme-substrate catalysis, polymerization, materials failures, phase changes in liquid crystals, metals and composites, droplet atomization processes, and elastic deformations of materials under stress (Gruner, 1987; Moffat, 1989, 2001). In many of these time-resolved experiments, the fundamental limitation is the lack of large-area X-ray imaging detectors with microsecond time resolution capabilities.

CCD-based detectors (Gruner *et al.*, 2002) commonly employed at synchrotron radiation sources are ill-suited for time-resolved experiments which require multiple two-dimensional images in rapid succession, or where a narrow time-window must be imaged at rates faster than typical mechanical shutters can readily gate the X-ray beam. Phosphor-coupled CCD detectors typically exhibit lag and afterglow on millisecond time scales, which limit the ability to see successive microsecond events (Shepherd *et al.*, 1997). CCD detectors that dispense with the phosphor, and use the silicon of the CCD as the medium to stop X-rays and create signal, suffer from limited depletion depth, leading to low X-ray stopping power and inefficient quantum efficiency. And even if these limitations are overcome, it typically takes milliseconds to seconds to read out the CCD. CCD detectors are useful for capturing single isolated submillisecond events, but this requires gating the X-ray signal in synchrony with the event using, for example, a complex high-speed X-ray shutter.

Multi-wire proportional detectors can be read out very fast and have good noise performance, but when used with intense synchrotron radiation sources they suffer significantly from global count-rate limitations. This limitation may be overcome by increasing the number of readout channels, but it will also increase cost and complexity.

Pixel array detectors offer solutions to many time-resolved and count-rate limitations (Heijne & Jarron, 1989). The PADs discussed in this article are two-layered devices consisting of a monolithic array of X-ray sensitive photodiodes connected to a monolithic CMOS readout electronics layer (Gruner *et al.*, 2002). Each photosensitive diode element on the detection layer is connected by metal dots ('bump-bonded') to its corresponding dedicated electronics. This architecture not only allows very fast parallel detection of X-rays, but also allows local processing/storage of the captured X-ray signal. This parallel processing and readout capability gives PADs great flexibility in the design of electronics. An optimized X-ray detector for a given application can be designed according to the experimental requirements by implementing suitable electronics within the pixel. Moreover, the implementation of an input amplifier in each pixel, in close proxi-

mity to the radiation sensing diode, reduces noise associated with long wires and stray capacitance.

As opposed to older detector technologies, PAD development is relatively young and evolving rapidly: functional changes to the CMOS electronics to adapt a PAD to a new synchrotron radiation experiment are readily implemented using the commercially available integrated circuit infrastructure and industry-standard design tools. As opposed to CCDs, the complex circuits generally do not require dedicated fabrication processes. The ease of functional modifications makes various pixel architectures possible. For example, using a type of X-ray detection layer common to each of the following systems, it is possible to design CMOS pixels that count individual X-ray photons, or pixels that analog integrate the incoming X-ray flux. An attraction of PAD technology is the enormous versatility associated with variation of the CMOS electronics to perform in-pixel processing: an in-pixel converter might be used with counting front-ends to implement limited energy resolution; or multiple-sampling methods can be used with integrating front-ends for in-pixel noise reduction or background subtraction. In-pixel autocorrelation circuits might be implemented for dynamic scattering type experiments, or local time discriminators/phase detectors can be implemented for phase-sensitive experiments.

Based on the functionality of the CMOS electronics, PADs used for synchrotron radiation experiments can be classified into two major groups. In PADs that count photons digitally (DPADs), individual X-ray photons are detected and locally counted in each pixel as they arrive (Mikulec *et al.*, 2001; Bronnimann *et al.*, 2001; Datte *et al.*, 1999). In PADs with front-end analog photon-integrating electronics (APADs), the incident X-ray signal is analog-integrated and stored in-pixel as a resultant voltage or current (Barna *et al.*, 1995, 1997; Rossi *et al.*, 1999). At the end of the X-ray integration period, this voltage/current signal is digitized.

Each architecture has its own advantages and shortcomings: DPADs may have very high signal-to-noise ratios. However, this is generally true only for a limited instantaneous X-ray flux (often $<10^6$ X-rays s^{-1} $pixel^{-1}$), because the photon amplification and discrimination electronics takes time to function. Integrating detectors are inherently tolerant to a high incident X-ray flux; in fact, some of the integrating X-ray detectors described in this article have been successfully operated at instantaneous local counts rates of almost 10^{12} X-rays s^{-1} $pixel^{-1}$ (Rossi *et al.*, 1999). On the other hand, integrating detectors do not generally resolve individual photons unless the gain of the system is increased substantially, which, as a consequence, sacrifices much of the well depth. If the signal is to be analog-stored for times approaching 1 s, APADs must be cooled to limit dark current and well depth loss. In either type of PAD, the charge from X-rays that convert near a pixel boundary (within about 10 μm) will be collected in two or more pixels. Such charge-sharing events pose a difficulty for counting detectors where incorrect thresholds can lead to missed or double counts. By contrast, an integrating detector such as the APAD fully records the partial charge into the respective pixels for split events thereby making a correct measurement of the X-ray intensity in a given neighborhood.

Because of their very high instantaneous count-rate capability, APADs are very well suited for high-instantaneous-flux imaging applications. Different variations of integrating front-ends could help different kinds of experiments: for very fast experiments, an integrating front-end could be merged with an in-pixel storage/memory stage for 'flash' or 'rapid-fire' mode of operation. In this mode, a limited number of very fast images are analog stored in the pixel, after which a longer time period is required to read out the stored images. The time resolution of this kind of architecture will fundamentally be limited by the collection time of the detector layer (nanoseconds) and the time constant of the input amplifier (from $\sim$100 ns to microseconds, depending on the number of equivalent bits of depth required). With proper CMOS readout electronics it is possible to image $\sim$150 ns events at 14-bit depth.

Alternatively, for relatively slow experiments (with millisecond time resolution) an integrating front-end can be combined with an in-pixel dual-port storage stage for a continuous streaming mode of images with very short dead time between images. In this mode, one set of in-pixel analog storage buffers are used to integrate an image while the previous image is being read out from another set of storage capacitors. After the image is read out, very fast (ns) CMOS switches are actuated so as to store the image on the second set of capacitors, while the first set is now read out. We call this 'push–pull' mode because signal is being 'pushed' onto one set of capacitors while the previously acquired image is 'pulled' from the other set. The minimum image acquisition rate is set by the time required to read an image off the APAD chip. For such a pixel, integration of X-rays and readout of the previous frame is performed simultaneously, which can be used to increase the duty cycle of the detector to very nearly 100%. Below we describe test APADs where both flash and push–pull modes are implemented in the same pixel. This is very useful. For example, in a typical time-resolved experiment such a detector can be operated in its push–pull mode to provide a video-rate stream of images for alignment of the sample and in order to search for interesting events, after which it can be electronically switched to flash mode for microsecond image acquisition of a limited number of images.

An integrating detector operating in continuous readout mode will also be very suitable for experiments that require high duty cycle, like fine φ-slicing crystallography experiments. For many diffraction experiments, half or more of the total experiment time is spent with the shutter closed for detector readout. An improvement in readout time will obviously allow better utilization of synchrotron beam time (Abola *et al.*, 2000).

APADs have limited well depths set by the ratio of the maximum analog signal that can be stored to the analog signal stored per X-ray. In cases where the signal is analog stored as a voltage on an in-pixel capacitor, well depth is determined by the size of the integrating capacitance that could be fit inside the pixel and the signal-to-noise ratio desired for very low

dose images. The well depth limitation may be circumvented by implementing an integrating front-end combined with an in-pixel state machine: every time the capacitor is filled, a digital bit is added to an in-pixel counter and the capacitor is drained. This kind of mixed-mode (MMPAD) analog/digital pixel architecture, in principle, allows very integrating front-ends to reach very large dynamic range values. First prototypes of MMPAD implementations are described below.

This article is organized as a summary of the design, characterization and application of prototype APADs built by the Cornell detector group for time-resolved X-ray experiments. In sequence, we discuss prototype flash APADs and some of the applications to which these detectors have been applied, a small-format push–pull APAD, large-format APADs, and prototype MMPAD designs.

2. Cornell 100 × 92 pixel flash APAD

The Cornell 100 × 92 detector is a prototype APAD designed to acquire up to eight sequential images (*e.g.* frames) with microsecond exposure and inter-exposure time resolutions (Barna *et al.*, 1995, 1997; Barna, 1996; Rodricks *et al.*, 1996; Eikenberry *et al.*, 1998; Rossi *et al.*, 1999, 2000; Renzi, 2003; Renzi *et al.*, 2002). It consists of two dies solder bump-bonded together: the detection layer and the CMOS layer. The detection die is high-resistivity silicon patterned with a two-dimensional array of 100 × 92 X-ray sensitive diodes, each 150 µm × 150 µm on a side. The high-resistivity array fill factor is 100%, with adjacent diodes defined only by the electric fields resulting from the metallization on the bump-bonding side of the die. The silicon detection layer is 300 µm thick, covers an active area of approximately 15 mm × 13.8 mm and was manufactured by SINTEF (SINTEF Electronics and Cybernetics, Blinden, Oslo, Norway). The diode layer was biased to an over-depletion voltage of 60 V, resulting in an active X-ray absorbing region of almost 300 µm of silicon. Given the detector and readout multiplexer parameters for the fabrication run, the charge collection efficiency can be estimated to be near unity. The perimeter of the active detection area is surrounded by a 150 µm-wide guard ring to minimize edge leakage currents and improve breakdown robustness. For silicon, each 3.65 eV of stopped X-ray energy yields an electron–hole pair. Thus, a stopped 10 keV X-ray yields a signal of about 2750 electrons. By contrast, typical charge yields in a phosphor-coupled CCD detector are in the range of 10–100 electrons (Tate *et al.*, 1997; Gruner *et al.*, 2002).

The stopping power of 300 µm of silicon is 97% at 8.9 keV and is still roughly 50% at 15 keV. High quantum efficiency for higher-energy X-rays would require a detection layer of thicker silicon or one made of semiconductors of higher atomic number. GaAs detectors were made and tested (Sellin *et al.*, 2001). However, better quality GaAs than was available to us at the time would be needed for future detectors. Appropriate quality GaAs is being used by the European Space Agency for satellite instruments (Owens *et al.*, 2002).

Table 1
Measured characteristics of the 100 × 92 PAD device. Values given in terms of X-rays refer to equivalent numbers of 8.9 keV X-rays. One analog-to-digital converter unit (ADU) is 1/65536 of 10 V. From Rossi *et al.* (1999).

RMS read noise	2.0–2.8 X-rays pixel^{-1}
Dark current (253 K)	6.2–30 fA pixel^{-1}
Dark current (253 K)	16–77 X-rays pixel^{-1} s^{-1}
Full well capacity	17000 X-rays
Non-linearity (% full well)	<0.2%
Quantum efficiency	97%
Conversion gain	2.75 ADU X-ray^{-1}

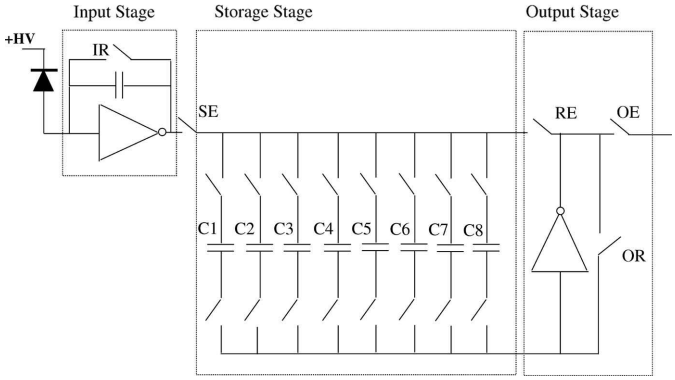

Figure 1
Simplified schematic of the pixel structure. Electronics integrated into each pixel of the readout integrated circuit (IC) are shown. Charge produced by the conversion of X-rays within the diode is integrated onto the capacitor in the input stage. Rapid imaging is accomplished by storing the integrated voltage level from successive images onto one of eight storage capacitors (C1–C8). Digital switching logic is used to select the desired capacitor. On readout, each capacitor is connected in succession to the output amplifier which is multiplexed to a buffer amplifier at the end of each pixel row. Also shown are various pixel control switches: IR, integrator reset; SE, store enable; RE, read enable; OE, output enable; OR, output reset.

The CMOS readout layer chip was fabricated *via* the MOSIS service (Information Sciences Institute, University of Southern California, Marina Del Rey, CA, USA) using a Hewlett-Packard (HP) 1.2 µm process. Bump-bonding of the silicon diode to readout electronics was carried out by GEC-Marconi (Caswell, UK). Detailed characterization of this detector has been presented elsewhere (Rossi *et al.*, 1999), and is summarized in Table 1. A simplified schematic of the electronics in each pixel is shown in Fig. 1.

Detector operation is performed in two steps: first the store enable (SE) switch is closed and the read enable (RE) switch is opened. Then one of the eight storage capacitors is connected to the integrator by switching its capacitor select line (C1–C8). The integrator reset (IR) switch is then opened and X-ray induced electrons are stored on the integrator/storage capacitors. At the end of X-ray integration time, the selected capacitor is disconnected from the circuit, and the IR switch is closed to reset the integration capacitor. Once this cycle is repeated for up to eight frames, a readout sequence is initiated by opening the SE switch and closing the readout enable (RE) switch. Then all stored capacitor voltages are sequentially read out through the output stage of each pixel.

The buffered voltage is digitized by an off-chip analog-to-digital converter (ADC). Note that integration is enabled only when the IR switch is open, allowing high-speed electronic shuttering of the X-ray signal. In addition, the switching can be operated in synchrony with the synchrotron bunch structure, allowing the isolation of individual X-ray bunches within the integration window, improving the minimum time resolution of the system to the bunch width of the synchrotron ring.

2.1. Application example: microsecond time-resolved radiography of fuel injector sprays

The ability of APAD analog integrating front-ends to handle high instantaneous count rates makes them good candidates for high-flux time-resolved radiography experiments. In this section we describe two applications of the Cornell 100 × 92 PAD to record ultra-fast X-radiography of highly transient fuel injector sprays. The experiments are the result of a collaboration with Dr Jin Wang's group at Argonne National Laboratory.

High-pressure high-speed sprays are essential for many applications, such as fuel injection systems, thermal/plasma spray coating, and liquid jet machining. Liquid sprays are often difficult to study using visible photons owing to intense multiple scattering from the fog of spray droplets. X-ray radiography, on the other hand, offers a good alternative as it is directly sensitive to the spray mass and penetrates even dense fogs.

Specifically, for fuel spray injector systems, understanding the details of atomization and dynamics of the sprays is of great importance towards increasing engine/fuel efficiency and reducing pollutants. Quantitative spray characterization has been a difficult task, as it requires microsecond time resolution experiments on sub-millimeter scale structures using complex liquid/gas mixtures. Previous X-ray radiography work on these systems had used point-by-point measurements of monochromatic X-ray absorption to characterize the dynamics of the fuel sprays (Powell *et al.*, 2000). While this technique allowed good time resolution, it is impractically laborious for imaging fuel sprays several centimeters across. The difficulty is compounded for topographic measurements, which require many snapshots of the spray taken from various angles. Area detectors allow much higher experimental throughput.

Several fuel injector systems have been studied using the 100 × 92 PAD. In one experiment we studied the dynamics of a common-rail diesel fuel injector (Powell *et al.*, 2000; MacPhee *et al.*, 2002; Renzi *et al.*, 2002). The injector system was similar to a passenger car injection system except that it has a specially fabricated single-orifice nozzle. The experiments were performed at the CHESS D1 beamline with 6 keV X-rays. The injection pressure of the fuel was varied from 50 to 135 MPa. The injection liquid was #2 diesel oil doped with a cerium compound to increase contrast. Fuel was injected into a chamber filled with inert SF_6 gas, which eliminated the explosion hazard, and whose density at 1 atm simulated the dense air environment of a diesel cylinder compression cycle.

Fig. 2 shows the time evolution of fuel spray from 38 to 192 µs after the start of injection at 135 MPa. The leading-edge speed of the spray reached 340 m s^{-1}, which exceeded the speed of sound in the SF_6 environment. The Mach cone of the shock wavefront generated by the supersonic fuel spray had an absorption contrast as high as 3% and was clearly visible. Despite significant experimental and theoretical studies, high-pressure fuel spray has not been recognized as supersonic under typical fuel injection conditions.

A second set of studies used the 100 × 92 PAD to image the three-dimensional and time-resolved dynamics of sprays in a hollow-cone gasoline direct injection system designed by Dr Wang's group (Renzi *et al.*, 2002; Renzi, 2003; Cai *et al.*, 2003). A detailed analysis of the fuel spray transient is of great importance for optimizing engine and fuel efficiency. An experimental set-up is shown in Fig. 3. A stainless steel cylindrical spray chamber was used with X-ray transparent windows that provided 120° of viewing angle. The fuel injection pressure for this experiment was 7 MPa with a nominal spray duration of 1 ms. The experiment was performed at the CHESS D-1 beamline using 6 keV X-rays with nominal beam size 15 mm × 2 mm, corresponding to 92 × 15 pixels on the PAD. The injection liquid was a blend of a gasoline-simulating calibration fluid doped with a cerium additive to increase fuel spray contrast. The spray chamber was designed to rotate at precise steps to allow data collection at different angles for tomographic reconstruction. This experiment resulted, for the first time, in a true three-dimensional time-resolved view of the entire injection cycle (*e.g.* see Fig. 4) (Cai *et al.*, 2003; Liu

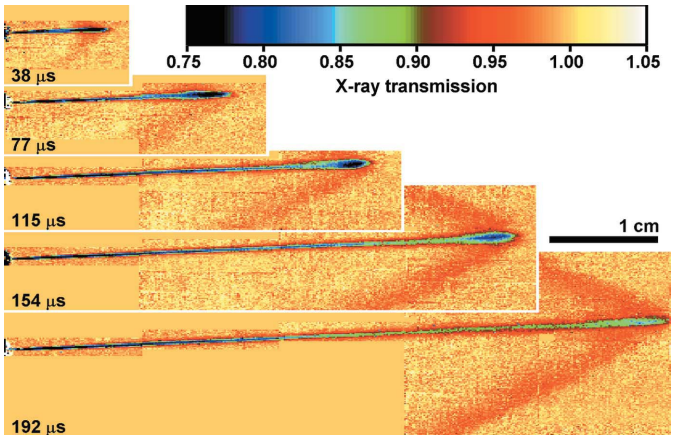

Figure 2
Time-resolved radiographic images of a supersonic jet of diesel fuel spray travelling through 1 atm of SF_6 gas. Shown are the fuel jet and the Mach cone for time instances of 38, 77, 115, 154 and 192 µs after the start of the injection. The imaged area shown in the largest panel is 61.7 mm (H) by 17.5 mm (V). Images are built up as a mosaic of 13.5 mm (H) by 2.5 mm (V) tiles by shifting the position of the fuel injector relative to the beam and the PAD and repeating the injection cycle. Boundaries between these areas can be seen upon close inspection. Images from some tile positions were not acquired. The exposure time per frame was 5.13 µs with data averaged over 20 injection cycles. The contrast of the shock wave was low, corresponding to only an average of about 15% increase in gas density near the shock front. (From MacPhee *et al.*, 2002.)

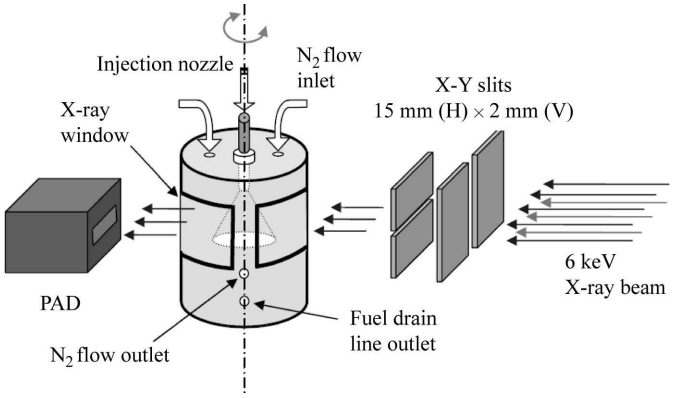

Figure 3
Schematic of the gasoline fuel injection experimental set-up. The X-ray beam from the CHESS D-1 beamline is monochromated to 6.0 keV using a double-multilayer monochromator and collimated to 15 mm (H) × 2 mm (V) by a set of slits. The gasoline fuel injector is mounted vertically along the rotation axis of an injection chamber having X-ray transparent mylar windows. Nitrogen flow at 1 atm is used to scavenge fuel vapor. Time-resolved tomographic data are acquired by recording time-resolved radiographs at each of a number of projection angles using the PAD. (From Liu *et al.*, 2004.)

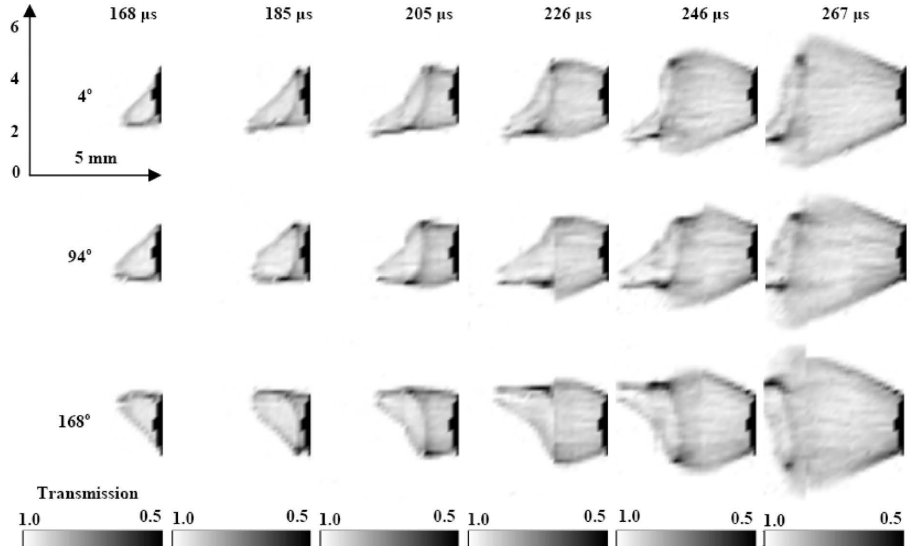

Figure 4
Radiographic images of the hollow-cone gasoline direct injection fuel sprays at projection angles of 4°, 94° and 168° and at various time instances after the start of the injection. Exposure time for each frame was 5.13 µs. Various details of the dynamic characteristics of the spray (density waves, asymmetry, streaks) can be identified from the images. (From, Liu *et al.*, 2004.)

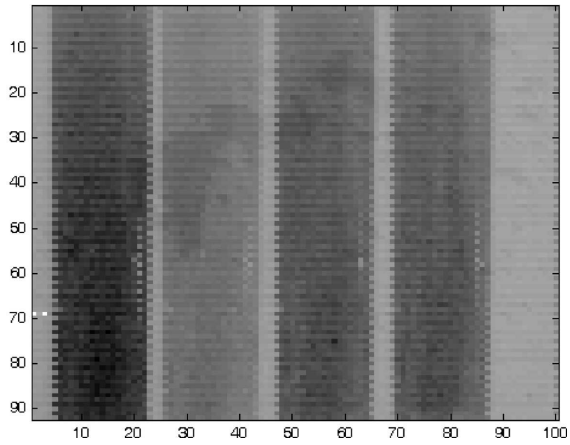

Figure 5
Radiation damage to a 92 × 100 detector used in fuel-spray radiography experiments. Shown is an image taken with zero X-ray dose. The four darker rectangular regions are regions which have received significant radiation dose and have become damaged, shifting the zero dose level by as much as 30% of full well capacity. The light-colored regions are normal undamaged areas. The boundaries of the damaged regions show an odd/even row pattern due to the asymmetric layout of the pixel electronics in the CMOS chip.

2.2. Shortcomings of the 100 × 92 PAD design

Experience gained from these experiments clearly demonstrated three shortcomings of the 100 × 92 PAD. Exposed regions of the detector chips showed significant radiation damage effects after 30 krad (referred to the CMOS gate SiO_2) of X-ray dose (Renzi *et al.*, 2002; Renzi, 2003). Integrated X-ray signal is stored as a voltage on an in-pixel capacitor. X-ray damage limits the available maximum voltage swing on this capacitor by two mechanisms (Anelli, 2000). First, X-ray absorption in the CMOS gate-oxides induces shifts in the threshold voltages of the transistors. Second, X-ray absorption in field oxides increases leakage currents between otherwise isolated CMOS devices. These two effects in turn shift the pedestal level of the integrating amplifier and limit the voltage swing on the integration capacitor.

Fig. 5 shows a typical background image taken with one of the detectors that had been radiation damaged after extensive use for the above-described fuel spray experiments. Each dark rectangular strip (of 92 × 13 pixels) corresponds to a region which received X-ray damage during the radiography experiments. Damaged areas showed well depth losses approaching 30% of full-well capacity. During fuel-spray radiography experiments, when one region became damaged, the detector was displaced and an undamaged region of the detector was used to collect the next set of experimental data.

et al., 2004). These data revealed important and previously unknown instabilities and asymmetries of the sprays, including density waves, streaks, an asymmetric cone shape, and non-uniform distribution of the fuel. Subsequent experiments (data in preparation) are being used to help design new types of injectors.

Although the 100 × 92 PAD was a test prototype never intended for dedicated use, it has proven to be a very useful tool for real-world applications. Other planned applications include observation of transient phase transitions in liquid crystals and metal composites.

Table 2
Measured device characteristics for 16 × 16 detectors. Values given in terms of X-rays refer to equivalent numbers of 8.9 keV X-rays. One analog-to-digital converter unit (ADU) is 1/65536 of 10 V. From Renzi (2003).

RMS read noise	4.3 X-rays pixel^{-1}
Dark current (253 K)	$<$50 fA pixel^{-1}
Dark current (253 K)	100 X-rays pixel^{-1} s^{-1}
Full well capacity	21 100 X-rays
Non-linearity (% full well)	$<$1.2%
Quantum efficiency	97%
Conversion gain	2.2 ADU X-ray^{-1}

For the detector shown in Fig. 5, four such movements were performed. Annealing the detectors at 373 K for 60 h reduced the radiation-damage-induced background shift; however, recovery was minor. While annealing will extend the useful life of these devices, much better radiation tolerance is expected from the smaller feature-size fabrication technologies which use thinner gate oxides.

Another observed problem was the pedestal level instability of the pixel, which contributed to the noise of the detector. This problem was more pronounced when the PAD was exposed to very high X-ray fluxes during radiography experiments ($>10^9$ X-rays pixel^{-1} s^{-1}). This problem was traced to the use of a single-ended amplifier for the integrating stage. To improve stability and noise performance, a differential amplifier-based integrating stage was considered for future detectors (Renzi, 2003; Eikenberry *et al.*, 1998). A third feature was the different behaviors observed on odd/even pixels of the detector. This is seen as the 'saw-tooth' edges in Fig. 5. This was due to the asymmetric pixel layout on the CMOS electronics, *e.g.* the CMOS pixel is a different shape from the detection layer pixel and does not sit directly under the detection pixel. This asymmetry affected the gain and radiation response of the pixels (Rossi *et al.*, 1999). It is easily resolved by a symmetric layout of the CMOS die.

3. 16 × 16 radiation-tolerant flash/push–pull APAD

Recent Cornell APAD designs have addressed the three problems indicated above. The radiation damage problem is now well understood and may be addressed by a combination of a deep submicrometer CMOS fabrication process and modified layouts of the MOS transistors (Jarron *et al.*, 1999; Anelli *et al.*, 1999; Anelli, 2000). Accordingly, recent Cornell PADs have all been fabricated using the commercially available 0.25 µm Taiwan Semiconductor Manufacturing Corporation (TSMC) process using enclosed layout transistors. Studies have also been carried out on the X-ray dose tolerance of various amplifiers and integrating pixels using enclosed layout gates (Renzi, 2003). The pixel stability problem was addressed by designing a differential integrating input stage amplifier with better noise/stability behavior. Finally, all pixels on the CMOS layer in recent designs have square pixels that are identical in size and shape to the pixels on the detection layer.

As an example, we describe a 16 × 16 pixel test APAD that combines the above-mentioned improvements with a push–pull architecture. The CMOS die was fabricated with a TSMC 0.25 µm process *via* the MOSIS service and the high-resistivity silicon detection layer was fabricated by SINTEF. The CMOS electronics were laid out using radiation-tolerant enclosed-layout transistors with 150 µm square pixels. A simplified pixel schematic is shown in Fig. 6.

In operation, one of the five capacitors, *e.g.* C0, is connected to the integrator by closing switches to the write bus and the SE switch. At the same time, another capacitor, *e.g.* C4, is connected to the output amplifier by closing CMOS switches to the read bus and switch RE. This allows C4 to be read out while integration occurs on C0. At the end of the integration, the capacitors are switched to reverse roles, *e.g.* C0 is read out while C4 integrates new signal. This operating mode allows continuous data collection with a duty cycle limited only by the time needed to reset the integration amplifier. The pixel could also be operated in flash mode with submicrosecond framing capability for five frames by deferring readout until all five capacitors per pixel have been sequentially filled, in a manner exactly analogous to the operation of the 100 × 92 PAD. A summary of the detector specifications is outlined in Table 2. Spatial resolution of the detector is measured as near ideal. With an X-ray spot of diameter 25 µm centered on a given pixel, no signal could be measured in the surrounding pixels at the 0.2% noise level of the measurement.

Fig. 7 shows the dramatically improved X-ray dose tolerance of the detector relative to the 100 × 92 PAD. Only a minor shift in the operating point of the detector is observed even after tens of Mrad of exposure. This shift is easily correctable using standard image calibration.

This prototype detector was successfully operated both in the flash and push–pull modes. In the push–pull continuous framing mode, frame rates approaching 150 Hz were easily achieved, limited only by the available off-chip readout elec-

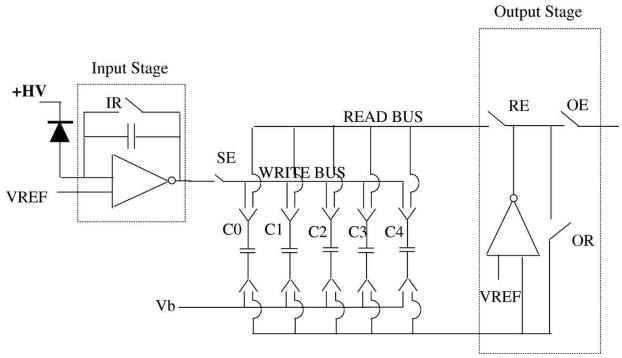

Figure 6
Simplified pixel schematic of the TSMC 0.25 µm 16 × 16 prototype PAD. This pixel can be operated in rapid-fire mode in the same manner as the 100 × 92 detectors with five instead of eight storage frames. Alternatively, it can be operated in push–pull mode, where any two of the capacitors (C0–C4) can be used for continuous write/read operation. Integrating onto one capacitor while a second capacitor is being read out, followed by a rapid reset and switch, allows nearly zero duty cycle operation. The duty cycle is limited by the reset time of the integrating front-end, which is approximately 1 µs.

tronics. Detailed electronic and X-ray characterization of this small prototype array will be discussed in a future publication.

4. 213 × 209 pixel large-format detectors

The 100 × 92 APAD was designed as a prototype detector and is limited in area coverage by the maximum allowed die size of the process used for the readout chip (15 mm × 15 mm). It also has wire bonding pads on four sides, which makes it difficult to tile a larger area with adjacent dies. For many applications it will be necessary for PADs to cover larger areas with more pixels. Towards this goal, a large-area APAD was designed and fabricated using the TSMC 0.25 μm process. This process allows a die area of about 21.5 mm × 21.5 mm which, with 100 μm square pixels, yields an array size exceeding 200 pixels in both dimensions. In order to cover large areas by tiling, the dies were designed to be butted against one another on three sides, with the remaining side for wire-bonding. Fig. 8 shows four CMOS dies bump-bonded to a single large diode layer. Diode detection layers for this detector were also manufactured at SINTEF. These 4 × 1 modules are intended to be stacked on top of one another in such a way that each module shadows the wire-bonded electronics of the modules underneath it, thereby covering a large area for normally incident X-rays. This scheme not only allowed a single large (852 × 209 pixels) detector module but also minimized dead space between detectors. A comparison of these detectors with the 100 × 92 detector can be seen in Fig. 8, with all detectors shown on the same scale.

Continued work on these detectors will be dependent on further funding. The units that have been bump-bonded to date (Advanced Interconnect Technologies, Hong Kong) have had poor bump-connection yields, but we are hopeful that the bump-bonding process has been improved. The CMOS dies also need to have a correction to the biasing network, which might require post-fabrication processing. Even so, preliminary visible light test of these detectors showed promising results. Detailed X-ray testing at the Cornell High Energy Synchrotron Source (CHESS) is currently ongoing.

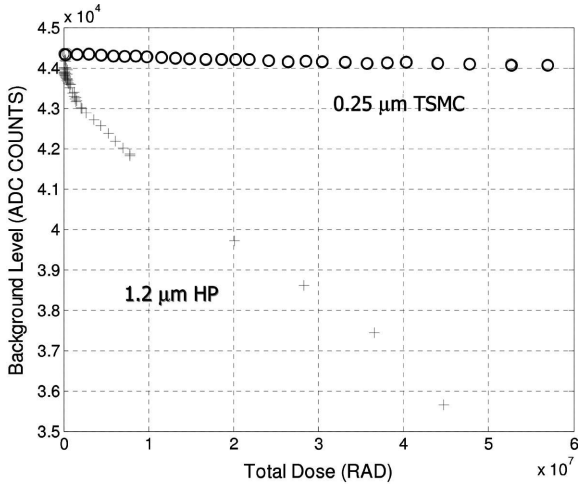

Figure 7
Changes in the background levels of the HP 1.2 μm 100 × 92 and TSMC 0.25 μm 16 × 16 prototype detectors for increasing radiation dose. Dose is referred to the front of the diode detection layer. The 100 × 92 detector was irradiated with 8.9 keV X-rays while the 16 × 16 detector was dosed using 8 keV X-rays. The radiation-induced shift in background level is primarily due to gate oxide charging in transistors within the pixel electronics. For the 100 × 92 detector, clear damage effects can be seen below 1 Mrad. Significant improvement in the background stability can be seen for the 16 × 16 prototype manufactured using a 0.25 μm process along with an enclosed layout technique for transistors. (From Renzi, 2003.)

5. Wide-dynamic-range integrating PAD

The well depth of the 100 × 92 APAD spans about four orders of magnitude, not too different from that of most CCD

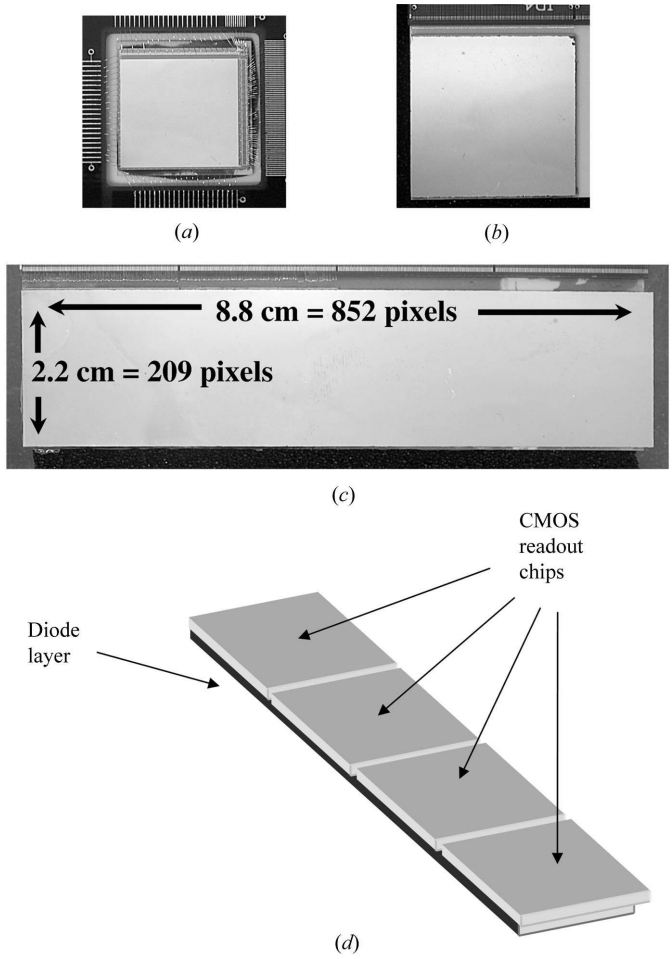

Figure 8
Evolution of Cornell integrating PADs for large area coverage. (*a*) The 100 × 92 pixel prototype was manufactured using the HP 1.2 μm process (now phased out) with 150 μm pixel size. Maximum die size for that process was limited to 15 mm × 15 mm. (*b*) New detectors were manufactured using the TSMC 0.25 μm process, which allows a maximum die size of ∼21.5 mm × 21.5 mm. In addition to improved radiation tolerance, small fabrication feature sizes allowed 100 μm pixels, yielding a detector of 209 × 213 pixels. These detectors were designed to be three-side buttable, with wire bonds on the fourth side. (*c*) 8.8 cm × 2.2 cm monolithic detector array. Four of the detector modules described in (*b*) above are bonded to a single diode array yielding a detector which is 209 × 852 pixels. These monolithic 4 × 1 modules can be tiled to cover even larger areas. (*d*) Schematic of the detector described in (*c*) showing four CMOS readout chips bonded to a single large diode array.

detectors. However, it is not unusual for an X-ray image to encompass features that differ by six or eight orders of magnitude in intensity, well beyond what can be easily accomplished with most simple analog storage schemes. This is often cited as an argument in favor of photon-counting PADs, where the range of recorded intensities is limited by the number of bits in the digital word of the detector.

This line of reasoning misses an important point. The analysis of X-ray images most commonly requires knowledge of the ratio of the X-ray intensities for two given locations in the image. The accuracy of this ratio is usually limited by the flat-field calibration of the detector, which is very rarely better than a few tenths of a percent and, for most commercial detectors, not much better than a percent (Barna *et al.*, 1999). This is true for both photon-counting and analog detectors, and is a result of variations in pixel sensitivity, X-ray windows, parallax considerations *etc.* Thus, what is really desired of most detectors is the ability to simultaneously capture features that differ by many orders of magnitude in intensity, while, as a practical matter of what people have actually done to process image data, it is usually sufficient to know the relative intensity to an accuracy of no more than a half percent. Alternatively stated, most users are satisfied (whether they realise it or not, because this is what they have actually been getting, in even the best cases) if the image data were delivered as an array of decimal floating point numbers with an 8-bit mantissa and a 3- or 4-bit exponent.

Accordingly, we designed a new integrating pixel architecture that combines the strong features of both integrating and counting detectors; that is, a wide well depth of counting pixels with high-count-rate tolerance of integrating front-ends. Here, an integrating front-end is combined with an in-pixel counter and state machine, which resets the integration capacitor every time the analog front-end saturates and adds an additional bit into an in-pixel digital counter. In other words, instead of counting X-rays, one counts the number of analog capacitor 'fills', each of which is equivalent to some fixed mean number of X-rays. At the end of the integration period, both the residual analog signal from the integrating front-end and the number of bits stored in the digital counter are read out. A block diagram of this 'mixed-mode pixel' is shown in Fig. 9. Note that the idea of digitally counting composite analog units of signal is not a new idea (Gottschalk, 1983) and, in effect, the MMPAD simply is the intermediate case between DPADs (which necessarily digitize an analog input signal) and APADs. But to our knowledge the MMPAD idea has not been implemented in a large-format X-ray detector. Nor has there been a general appreciation that such a device might provide data at least as accurate as from both more traditional analog integrating and digital photon-counting detectors.

In practice, the mixed-mode pixel operates as follows. An in-pixel comparator constantly compares the integrating front-end voltage with a reference threshold voltage which corresponds to some preset value less than the saturation voltage of the charge integrator. When the integrated X-ray dose reaches this threshold voltage, a bit is added into an in-pixel digital counter and the integrator stage is reset for continued analog integration. At the end of the desired integration period, the number stored in the digital counter is read out and, for increased accuracy, the residual analog signal on the charge integrator is digitized. By appropriate selection of the reference voltage of the threshold detector, this pixel architecture is capable in principle of reaching very high dynamic ranges while maintaining a tolerance for very high local count rates. Such a detector would be useful for many small-angle X-ray scattering experiments where the scattered signal often spans a high dynamic range.

A prototype 16 × 16 array based on a mixed-mode PAD was designed and manufactured using the TSMC 0.25 µm five-metal MiM-cap non-epi process. Each pixel in this prototype was 150 µm square, resulting in a 3.6 mm × 3.7 mm total die size. Each pixel contained an integrator, a threshold

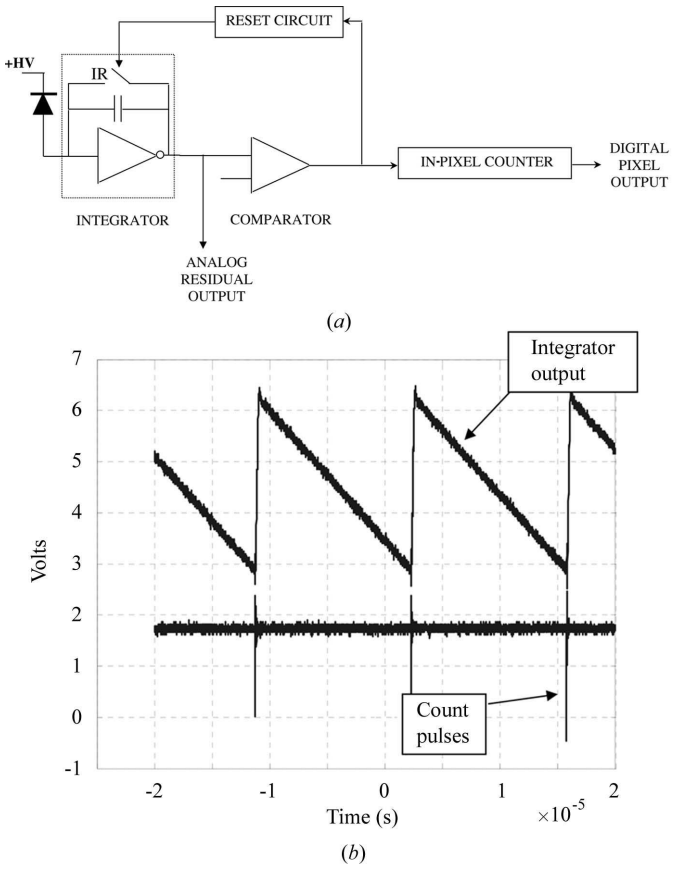

Figure 9
(*a*) Block diagram of the mixed-mode pixel. During the integration period, the voltage at the integrator output is continuously compared with a threshold level. When this level is reached, an in-pixel counter is incremented and integrator stage is reset for the next cycle. At the end of the X-ray integration period, both the residual analog voltage of the integrator stage and the digital counts corresponding to the number of overflows is read out. Such a structure retains the high-count-rate capability of an integrating detector while extending the single-frame dynamic range significantly. (*b*) Oscilloscope plot from the first functional mixed-mode pixel; the triangular wave is the integrator stage output. The second trace is the count pulse sent to the in-pixel counter whenever an analog overflow occurs. Preliminary tests showed good linearity and stability; however, noise performance, especially during reset phase, required improvements.

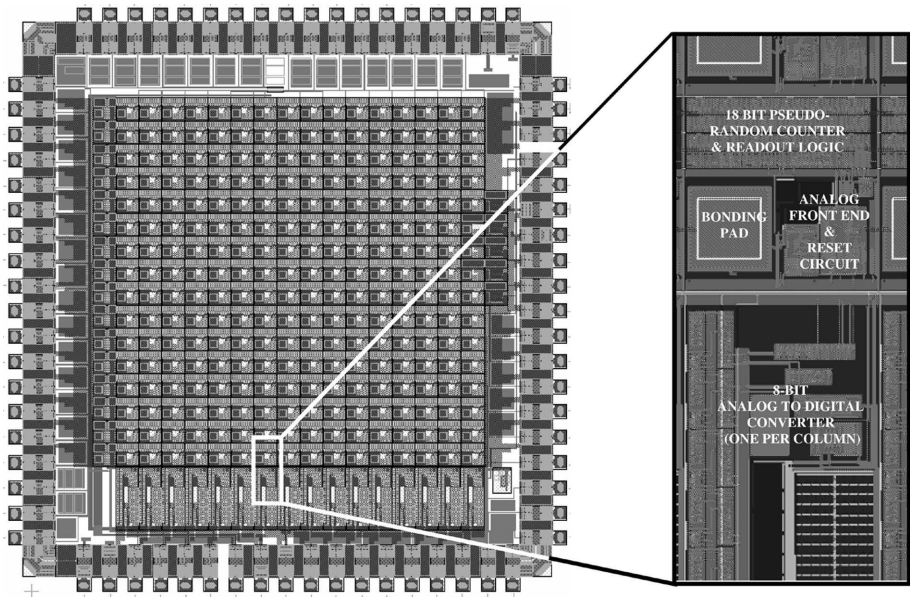

Figure 10
Layout of the first mixed-mode pixel array prototype. This ASIC was manufactured using the TSMC 0.25 μm five-metal thick-oxide MiM process on non-epi substrate *via* MOSIS service. The ASIC consists of a 16 × 16 array of mixed-mode pixels and 16 on-chip 8-bit ADCs which were arranged in one-per-column format. This prototype was designed to give digital-only output, with the on-chip ADCs used to digitize the residual analog signal (see Fig. 9) at the end of the integration period. Variations of the mixed-mode pixel were distributed inside the array. Die size is 3.6 mm × 3.7 mm with approximately 185 000 transistors. Pixels are 150 μm square and consist of an integrator front-end, a comparator, 18-bit pseudo-random counter and reset/readout logic. On-chip ADCs used successive approximation architecture and occupied approximately 150 μm × 400 μm die area. Significant pixel area was consumed by the bump-bonding pad, which was required due to the special bump-bonding technique used for this prototype.

comparator, an 18-bit pseudo-random counter and logic circuit to control reset operation. The ASIC (application-specific integrated circuit) also contained 16 eight-bit on-chip ADCs, arranged in a one-per-column configuration, to digitize the residual analog signal from pixels on the chip. The layout of this prototype mixed-mode PAD (MMPAD) is shown in Fig. 10. Bump-bonding of this prototype was performed by ADSC (Area Detector Systems Corporation, Poway, CA, USA). Initial tests of this detector showed very promising results. A sample pixel waveform is shown in Fig. 9. Further work is necessary to realise the potential of a large-area MMPAD. For example, careful attention needs to be given to the reset noise when resetting the capacitor. A discussion of our mixed-mode pixel work to date has been presented (Angello *et al.*, 2005).

6. Conclusion

The focus of this article has been on the diode detection layer and CMOS chips that are at the heart of a PAD. The promise of X-ray PADs follows from two facts: (i) modern CMOS electronics offers great flexibility of function, and (ii) the high quality of detector-grade semiconductors are superior converters of X-rays to electrical signals. Many considerations and components must additionally be dealt with in order to have useful detectors, including chip tiling and packaging, cooling, off-chip electronics, software, calibrations *etc.* In practice, the detector designer spends a very large amount of effort integrating all these aspects into a working detector.

The development of a new X-ray detector technology is typically decades long (Gruner, 1999). Fabrication of large-area CMOS chips is inherently expensive, often costing $100 000 to $200 000 per fabrication. The development of a large-area PAD requires several such fabrications. Thus, PAD technology requires a large commitment of resources for a very long time. Fortunately, IC fabrication obeys an economy of scale: once developed, the unit cost of a chip is relatively low. The X-ray detector community is climbing the learning curve required to build useful PADs. Several PAD groups around the world are near to the point at which economies of scale set in. Given sufficient resources for continued development, we predict that commercially available PADs should begin to appear within a decade, and will become amongst the most important detectors in the decade after.

The PAD work described in this article is the result of the work of many people. We wish to acknowledge Sandor Barna, Eric Eikenberry, Matt Renzi, Giuseppe Rossi and Bob Wixted for their roles in the development of the 100 × 92 PAD; Paul Sellin and A. P. Knights for the GaAs tests; Jin Wang and his collaborators for the fuel-injector radiography experiments; Ernie Fontes and the CHESS staff for help with experiments at CHESS; collaborators at Area Detector Systems Corporation (ADSC; Susan Angello, Skip Augustine, Tom Hontz, Ron Hamlin, Wayne Vernon) for work on the MMPAD; and the recent and present members of the Cornell Detector Group (Darol Chamberlain, Lucas Koerner, Hugh Philipp and Dan Schuette) for involvement in many PAD activities. Support for our detector development at Cornell has come from US Department of Energy (DOE) grant DE-FG-0297ER1485, US National Institutes of Health (NIH) grant RR014603 to ADSC, and, especially, the DOE-BER grant DE-FG-0297ER62443. CHESS, where much experimentation has been performed, is supported by the US National Science Foundation and NIH-NIGMS *via* grant NSF DMR-0225180.

References

Abola, E., Kuhn, P., Earnest, T. & Stevens, R. C. (2000). *Nature Struct. Biol.* **7**, 973–977.

Anelli, G., Campbell, M., Delmastro, M., Faccio, F., Florian, S., Giraldo, A., Heijne, E., Jarron, P., Kloukinas, K., Marchioro, A., Moreira, P. & Snoeys, W. (1999). *IEEE Trans. Nucl. Sci.* **46**, 1690–1696.

Anelli, G. M. (2000). PhD thesis, Institut National Polytechnique de Grenoble, France.

Angello, A. G., Augustine, F., Ercan, E., Gruner, S. M., Hamlin, R., Hontz, T., Renzi, M., Schuette, D., Tate, M. & Vernon, W. (2005). *IEEE Trans. Nucl. Sci.* In the press.

Barna, S. (1996). PhD thesis, Princeton University, USA.

Barna, S. L., Shepherd, J. A., Tate, M. W., Wixted, R. L., Eikenberry, E. F. & Gruner, S. M. (1997). *IEEE Trans. Nucl. Sci.* **44**, 950–956.

Barna, S. L., Shepherd, J. A., Wixted, R. L., Tate, M. W., Rodricks, B. & Gruner, S. M. (1995). *Proc. SPIE*, **2521**, 301–309.

Barna, S. L., Tate, M. W., Gruner, S. M. & Eikenberry, E. F. (1999). *Rev. Sci. Instrum.* **70**, 2927–2934.

Bronnimann, C., Baur, R., Eikenberry, E. F., Kohout, S., Lindner, M., Schmitt, B. & Horisberger, R. (2001). *Nucl. Instrum. Methods Phys. Res. A*, **465**, 235–239.

Cai, W., Powell, C. F., Yue, Y., Narayanan, S., Wang, J., Tate, M. W., Renzi, M. J., Ercan, A., Fontes, E. & Gruner, S. M. (2003). *Appl. Phys. Lett.* **83**, 1671.

Datte, P., Birkbeck, A., Beuville, E., Endres, N., Druillole, F., Luo, L., Millaud, J. & Xuong, N.-H. (1999). *Nucl. Instrum. Methods Phys. Res. A*, **421**, 576–590.

Eikenberry, E. F., Barna, S. L., Tate, M. W., Rossi, G., Wixted, R. L., Sellin, P. J. & Gruner, S. M. (1998). *J. Synchrotron Rad.* **5**, 252–255.

Gottschalk, B. (1983). *Nucl. Instrum. Methods Phys. Res. A*, **207**, 417–421.

Gruner, S. M. (1987). *Science*, **238**, 305–312.

Gruner, S. M. (1999). *Trans. Am.* **34**, 11–25.

Gruner, S. M., Tate, M. W. & Eikenberry, E. F. (2002). *Rev. Sci. Instrum.* **73**, 2815.

Heijne, E. H. M. & Jarron, P. (1989). *Nucl. Instrum. Methods Phys. Res. A*, **275**, 467–471.

Jarron, P., Anelli, G., Calin, T., Cosculluela, J., Campbell, B., Delmastro, M., Faccio, F., Giraldo, A., Heijne, E., Kloukinas, K., Letheren, M., Nicolaidis, M., Moreira, P., Paccagnella, A., Marchioro, A., Snoeys, W. & Velazco, R. (1999). *Nucl. Phys. B Proc. Suppl.* **78**, 625–634.

Liu, X., Liu, J., Li, X., Cheong, S.-K., Shu, D., Wang, J., Tate, M. W., Ercan, A., Schuette, D. R., Renzi, M. J., Woll, A. & Gruner, S. M. (2004). *Proc. SPIE*, **5535**, 21–28.

MacPhee, A. G., Tate, M. W., Powell, C. F., Yue, Y., Renzi, M. J., Ercan, A., Narayanan, S., Fontes, E., Walther, J., Schaller, J., Gruner, S. M. & Wang, J. (2002). *Science*, **295**, 1261.

Mikulec, B., Campbell, M., Dipasquale, G., Schwarz, C. & Watt, J. (2001). *Nucl. Instrum. Methods Phys. Res. A*, **458**, 352–359.

Moffat, K. (1989). *Annu. Rev. Biophys. Biophys. Chem.* **18**, 309–332.

Moffat, K. (2001). *Chem. Rev.* **101**, 1569–1581.

Owens, A., Bavdaz, M., Peacock, A., Andersson, H., Nenonen, S., Krumrey, M. & Puig, A. (2002). *Nucl. Instrum. Methods Phys. Res. A*, **479**, 531–534.

Powell, C. F., Yue, Y., Poola, R. & Wang, J. (2000). *J. Synchrotron Rad.* **7**, 356–360.

Renzi, M. J. (2003). PhD thesis, Cornell University, USA.

Renzi, M. J., Tate, M. W., Ercan, A., Gruner, S. M., Fontes, E., Powell, C. F., MacPhee, A. G., Narayanan, S., Wang, J., Yue, Y. & Cuenca, R. (2002). *Rev. Sci. Instrum.* **73**, 1621.

Rodricks, B. G., Barna, S. L., Gruner, S. M., Shepherd, J. A., Tate, M. W. & Wixted, R. L. (1996). *Rev. Sci. Instrum.* **67**, 3360.

Rossi, G., Renzi, M., Eikenberry, E. F., Tate, M. W., Bilderback, D., Fontes, E., Wixted, R., Barna, S. & Gruner, S. M. (1999). *J. Synchrotron Rad.* **6**, 1096–1105.

Rossi, G., Renzi, M. J., Eikenberry, E. F., Tate, M. W., Bilderback, D., Fontes, E., Wixted, R., Barna, S. & Gruner, S. M. (2000). *Synchrotron Radiation Instrumentation: Eleventh US National Conference (AIP Proceedings 521)*, edited by P. Pianetta, pp. 311–316. Melville, NY: AIP.

Sellin, P. J., Rossi, G., Renzi, M. J., Knights, A. P., Eikenberry, E. F., Tate, M. W., Barna, S. L., Wixted, R. L. & Gruner, S. M. (2001). *Nucl. Instrum. Methods Phys. Res. A*, **460**, 207–212.

Shepherd, J. A., Gruner, S. M., Tate, M. W. & Tecotzky, M. (1997). *Opt. Eng.* **36**, 3212.

Tate, M. W., Gruner, S. M. & Eikenberry, E. F. (1997). *Rev. Sci. Instrum.* **68**, 47–54.